INSTITUTE OF PHYSICS PUBLISHING PHYSICS IN MEDICINE AND BIOLOGY

Phys. Med. Biol. **51** (2006) 5889–5902 doi:10.1088/0031-9155/51/22/011

Influence of excitation light rejection on forward model mismatch in optical tomography

K Hwang[1], **T Pan**[1], **A Joshi**[1], **J C Rasmussen**[1], **W Bangerth**[2] **and E M Sevick-Muraca**[1]

[1] Department of Radiology, Baylor College of Medicine, Houston, TX 77843, USA
[2] Department of Mathematics, Texas A&M University, College Station, TX 77843, USA

E-mail: evas@bcm.tmc.edu

Received 19 July 2006, in final form 5 September 2006
Published 27 October 2006
Online at stacks.iop.org/PMB/51/5889

Abstract

Fluorescence enhanced tomography for molecular imaging requires low background for detection and accurate image reconstruction. In this contribution, we show that excitation light leakage is responsible for elevated background and can be minimized with the use of gradient index (GRIN) lenses when using fibre optics to collect propagated fluorescence light from tissue or other biological media. We show that the model mismatch between frequency-domain photon migration (FDPM) measurements and the diffusion approximation prediction is decreased when GRIN lenses are placed prior to the interference filters to provide efficient excitation light rejection. Furthermore, model mismatch is correlated to the degree of excitation light leakage. This work demonstrates the importance of proper light filtering when designing fluorescence optical imaging and tomography.

(Some figures in this article are in colour only in the electronic version)

1. Introduction

The development of near-infrared (NIR) excitable, optical imaging agents promises a new approach to molecular imaging that could rival the 'gold-standards' provided by scintigraphy, single photon emission computed tomography (SPECT) and positron emission tomography (PET). Recently, a number of cyanine dyes (Achilefu *et al* 2000, Licha 2002, Lin *et al* 2002, Pham *et al* 2003), that represent the most prominent class of NIR fluorophores, have been synthesized, and a few are commercially available. Fluorophores such as non-specific indocyanine green (ICG) and conjugatable NHS esters of cyanine dyes are stable, non-radioactive, and do not possess a physical half-life, making imaging agent design, synthesis and implementation convenient. Furthermore, Houston *et al* (2005) have recently employed an RGD dual-labelled peptide to show the superior signal-to-noise ratio (SNR) of optical over nuclear imaging in a subcutaneous xenograft model of human melanoma. The results can be explained by the ability to repeatedly re-excite the fluorophore with tissue-propagating NIR excitation light enabling as many as 10^9 imaging photon events per second per fluorophore as opposed to one relaxation for each nuclear isotope. However, owing to light attenuation, the comparison of NIR fluorescence with nuclear imaging techniques becomes less convincing when targeted tissues of interest are located deep within tissues.

Recently, we have demonstrated that the excitation light leakage through bandpass rejection filters creates a 'noise' floor that could restrict detection of emission light from picomolar amounts of NIR fluorophore deep within tissues (Houston *et al* 2003, Hwang *et al* 2005). Using planar, small animal imaging, we have recently shown that by collimating the image plane onto interference and holographic filters, target-to-background ratios (TBRs) improved by 30% (Hwang *et al* 2005). The result can be explained by the deteriorating rejection performance of interference and holographic filters as incident light deviates from the normal direction onto the filter. By collimating the image plane before passing through the rejection filters, TBR, a figure of merit of imaging agent selectivity, increased due to the improved filter performance and the enhanced efficiency collecting for weak fluorescent signals.

For detection of target tissues in clinically relevant volumes, three-dimensional optical tomography using point illumination of excitation light and fibre optic collection of generated fluorescence is employed (Godavarty *et al* 2004). Since time-dependent methods provide the greatest contrast (Sevick-Muraca *et al* 1997, Li *et al* 1998) and are less impacted by changes in endogenous optical properties (Eppstein *et al* 1999, Sahu *et al* 2005), herein we focus on fibre optic delivery of intensity modulated excitation light and fibre optic collection of generated fluorescence to experimentally demonstrate the use of gradient index (GRIN) lenses for efficient collection of weak fluorescence signals and rejection of excitation light. In this study, we adapt GRIN lenses into an existing frequency-domain tomography system to detect fluorescence signals from a clinically relevant breast phantom in the presence and absence of indocyanine green (ICG). To quantitate the improvement of tomographic information content, we compute the model mismatch errors of amplitude ratio (ACR) and relative phase difference (RPS) between fluorescent measurements with and without GRIN collimation and predicted values from a diffusion-based forward model under conditions of varying target depth and fluorophore concentration. This work shows that model match is improved by proper adaptation of GRIN lenses as collimating optics in fluorescence enhanced optical imaging.

2. Materials and methods

2.1. Breast phantom

Measurements were made using a large breast phantom of $\sim$1087 cm^3 volume as shown in figure 1(a). The hemispherical portion (10 cm inner diameter) of the phantom structure represents the breast tissue and the cylindrical portion (20 cm inner diameter and 10 cm height) of the phantom represents the extended chest wall regions and the tissues beneath the breast. A 0.5 cm phantom wall thickness enables the firm placement of illuminating source and collection fibres.

Multimode optical fibres (model FT-1.0-EMT, Romack Inc., NJ) of 1000 μm diameter and a 0.51 numerical aperture were used to illuminate and collect the excitation and emission light. A total of 26 sources and 128 collection fibres were glued (Mr. Sticky's underwater glue, Advanced Adhesion Inc., CA) symmetrically in concentric rings along the hemispherical

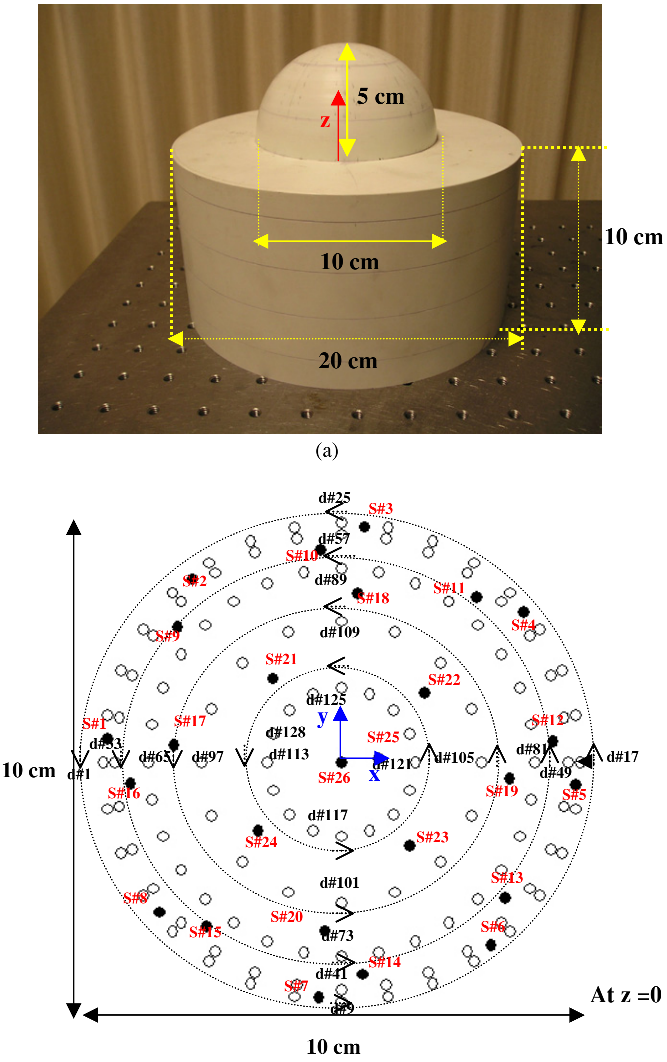

(a)

(b)

Figure 1. (a) 3D tissue-mimicking breast phantom and dimensions of the cup-shaped phantom; (b) *x*–*y* location of all 26 point illumination (filled circles) and 128 collection fibre locations (open circles) on the hemispherical portion of the breast phantom. S# and d# represent source and detector number respectively, with arrows indicating the numbering direction (counter-clockwise) of 128 collection fibres; (c) fibre bundle without grin lenses which is imaged onto the photocathode of the image intensifier. The distal ends of fibres collected light from the phantom as shown in figure 2.

portion of the phantom. Figure 1(b) shows the locations of 128 collection fibres and 26 source fibres mounted on the hemispherical portion of the phantom. Collection and source fibre numbers are listed for the results presented herein. The collection fibres terminated at a fibre bundle whose diameter was 80 mm. 128 collection fibre ends were evenly spaced 5 mm apart in the 60 mm diameter bundle face as shown in figure 1(c) for area imaging using an intensified charge coupled device (ICCD) camera.

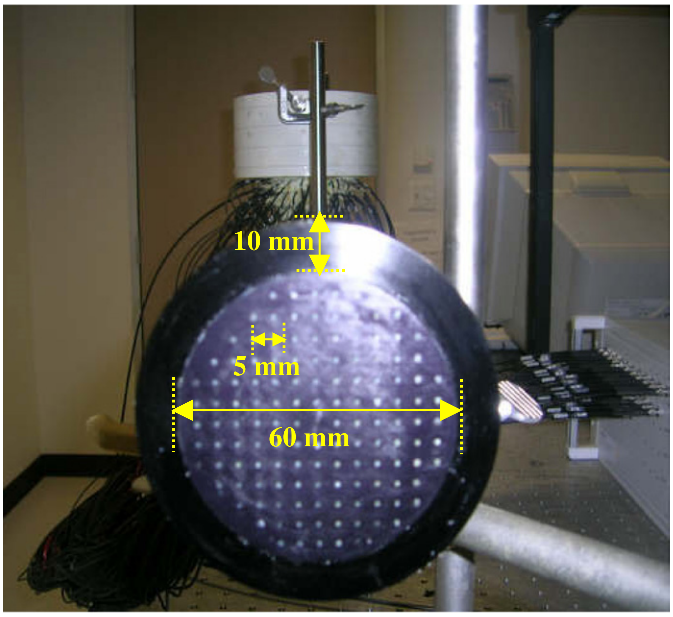

(c)

Figure 1. (Continued.)

The phantom was filled with 1% (by volume) Liposyn (Abbott Laboratories, North Chicago, IL) solution with measured optical properties of $\mu_s' = 10.31\ \mathrm{cm}^{-1}$ and $\mu_a = 0.025\ \mathrm{cm}^{-1}$ at the excitation wavelength of 785 nm and of $\mu_s' = 9.56\ \mathrm{cm}^{-1}$ and $\mu_a = 0.022\ \mathrm{cm}^{-1}$ at the emission wavelength of 830 nm. Frequency domain photon migration (FDPM) measurements were acquired at all detectors at the emission wavelength of 830 nm for each source of excitation light. The target consisted of a 1 cm^3 spherical glass bulb with its centroid located 1.26, 2, and 3 cm deep along the inward pointing normal of the phantom surface at (x, y, z) coordinates of (2, 1, 3), (2, 1, 2) and (0, 0, 2). The origin of the system is taken to be at the centre of the hemisphere base. Varying ICG target concentrations of 0.25 to 1 μM were investigated at a target depth of 1.26 cm. Measurements of amplitude and phase were acquired under TBR of 100:1.

2.2. Instrumentation

Frequency domain photon migration (FDPM) measurements were conducted using the ICCD homodyne detection system which is described elsewhere (Godavarty *et al* 2004, Thompson and Sevick-Muraca 2002, Reynolds *et al* 1997). As illustrated in figure 2, a 785 nm laser diode (HPD1105-9mm-D-78505 model, High Power Devices Inc., NJ), typically operated at 200 mW, was modulated at 100 MHz by a signal generator (Marconi Instrument Ltd., model 2022D, Hertfordshire, UK) to generate an intensity modulated excitation source. The source was delivered sequentially via an optical switch (LT 1100 Multi-Channel Switch, LIGHTech Fiberoptics, Inc., CA) and one of the 26 source fibres to the phantom surface. The collecting fibres delivered propagated excitation and emission light to the fibre bundle faceplate where a lens (50 mm f/1.8D AF NIKKOR, Nikon Inc, New York) focused the collected light on to the photocathode of an image intensifier (ITT Industries Night Vision, model FS9910C, Roanoke,

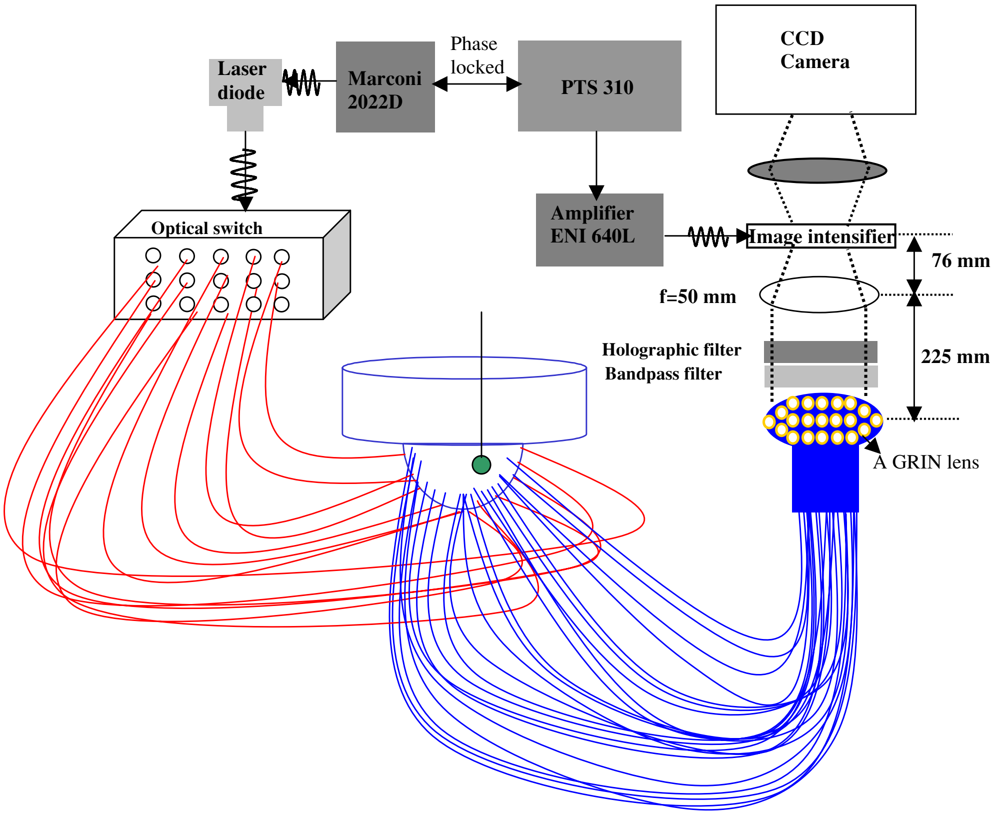

Figure 2. Instrumentation set-up of the tomographic imaging system and phantom.

VA). The photocathode of the image intensifier was modulated at 100 MHz by an amplified (amplifier model 604L, ENI Technology, Inc., Rochester, NY) sinusoidal signal from a PTS 310 (Programmed Test Sources, Inc., model 310, Littleton, MA) which was phase locked to the Marconi 2022D synthesizer. The intensified signal emitted from the image intensifier was focused onto a 16 bit cooled CCD camera (Photometrics Ltd., Series AT200, model SI512B, Tucson, AZ) where images were acquired and stored onto a computer. The images were subsequently processed to obtain the amplitude (I_{ac}) and phase (θ) of each collection fibre. I_{ac} and θ were then referenced to that from the fibre with the maximum amplitude.

A three-cavity, 830 nm bandpass filter with 10.33 nm full width at half maximum (830FS10-50, Andover, Salem, NH: optical density (OD) = 5.5 at 785 nm) and a holographic super notch filter plus (HSPF785.0-2.0, Kaiser Optical System, Ann Arbor, MI: OD $>$ 6.0 at 785 nm) were positioned prior to the photocathode of the image intensifier to reject the 785 nm excitation light and to pass the 830 nm emission light. In order to collimate the light emerging from the 128 collection fibres in the fibre bundle, custom-made GRIN lenses (SLW type, NSG America Inc., NJ) were glued to the ends of the collection fibres in the fibre bundle using optical adhesives (OP series, refractive index ~1.49, DYMAX Corporation, Torrington, CT). The GRIN lenses were designed from the Eikonal equation (Sakamoto 1993) for a lens length of 10.4 mm and a diameter of 4 mm based upon pitch and the gradient lens constant. Attenuation losses owing to the addition of the GRIN lenses at 830 nm are expected to be minimal since transmission efficiencies are 90–98%. The schematic of the instrumentation employed for investigating the improvement of excitation light rejection for optical tomography of the breast phantom is illustrated in figure 2.

2.3. Fibre calibration

We found that small differences in fibre lengths made reproducible contributions to the phase measurements while amplitude values were unaffected. To correct the systematic phase offsets, FDPM measurements were performed on a homogeneous phantom filled with a 1% intralipid solution with 0.01 μM ICG. The FDPM phase measurements were compared with forward model predictions and the difference between their relative phase shifts (RPS) was calculated as:

$$\mathrm{RPS}_{\mathrm{errors},i} = \mathrm{RPS}_{\exp,i} - \mathrm{RPS}_{\mathrm{sim},i} \tag{1}$$

where $\mathrm{RPS}_{\exp,i}$ and $\mathrm{RPS}_{\mathrm{sim},i}$ are relative phase shifts of experiments and simulations for each collection fibre, i. The $\mathrm{RPS}_{\mathrm{error},i}$ was determined with and without the GRIN lenses and fibre calibration was performed by subtracting the $\mathrm{RPS}_{\mathrm{error},i}$ from the phase measurements obtained when the target was present. Unless otherwise stated, all phase measurements are reported as ‘calibrated’ values.

2.4. Assessment of excitation light leakage

Measurements at the surface of the target-free breast phantom containing intralipid with and without ICG provided a method to assess excitation light leakage. Excitation light leakage is defined as the signal, $S(\lambda_{\mathrm{x}})$, or average pixel intensity values associated with the measurements taken in the absence of ICG in the solution when bandpass and holographic filters are used. The average pixel intensity represents the intensity averaged over all the pixels corresponding to the region of each collection fibre. The fluorescence signal, $S(\lambda_{\mathrm{m}})$, is likewise averaged from the pixel intensity values associated with the measurements taken in the presence of ICG in the solution. The $S(\lambda_{\mathrm{x}})$ signal represents ‘out of band’ transmission signals, whereas the difference, $S(\lambda_{\mathrm{m}}) - S(\lambda_{\mathrm{x}})$, when taken at the same intensifier gain, represents the ‘in-band’ transmission signal. The transmission ratio for each collection fibre is given by ($R(I_{\mathrm{dc}})$ or $R(I_{\mathrm{ac}})$),

$$R(I_{\mathrm{dc}}) \text{ or } R(I_{\mathrm{ac}}) = \frac{S(\lambda_{\mathrm{x}})}{S(\lambda_{\mathrm{m}}) - S(\lambda_{\mathrm{x}})} \tag{2}$$

where S is the signal measured either by the average intensity, I_{dc}, or the amplitude of intensity, I_{ac}. FDPM images of the fibre bundle enabled measurements of I_{ac} and I_{dc} at the ends of each collecting fibre using the homodyne procedure as described by Thompson *et al* (2003). Three binned images (128 × 128 pixels) were acquired each with 0.4 s of integration time as the phase delay between the RF driving the image intensifier and the laser diode was changed from 0 to 360°. Since the entire fibre bundle end was imaged, five pixels corresponding to each of the ends of collecting fibres were identified and processed for I_{ac} and I_{dc}. Values of $R(I_{\mathrm{dc}})$ and $R(I_{\mathrm{ac}})$ were calculated for each collection fibre with and without the GRIN lenses.

2.5. Assessment of model mismatch errors

The acquired fluorescence measurements of I_{ac} and phase at each collection fibre were referenced with respect to the collection fibre which exhibited the maximum amplitude for each source illumination. The referenced values at collection fibre (i) are calculated as shown in equations (3) and (4).

$$\mathrm{ACR}_i = I_{\mathrm{ac}i}/I_{\mathrm{ac,ref}} \tag{3}$$

$$\mathrm{RPS}_i = \theta_i - \theta_{\mathrm{ref}} \tag{4}$$

where ACR_i is the amplitude ratio, RPS_i is the relative phase difference, and $I_{\mathrm{ac,ref}}$ and θ_{ref} are the maximum amplitude and calibrated phase values respectively for each source illumination. Values of phase were calibrated as described in section 2.3.

Simulations of $I_{\mathrm{ac}i}$ and θ_i were obtained from the forward model of the coupled diffusion equations using an adaptive finite element method (Joshi *et al* 2004) to provide solution on a mesh with 35 000 hexahedral elements. The difference between the referenced measurement and simulated data is called the 'model mismatch error'. The model mismatch error is determined as the sum of the errors or differences between the experimental data and its corresponding simulated data as expressed for $\mathrm{ACR}_{\mathrm{error,\ sum}}$ and $\mathrm{RPS}_{\mathrm{error,\ sum}}$ by equations (5) and (6).

$$\mathrm{ACR}_{\mathrm{error,sum}} = \sum_{i=1}^{128} |\mathrm{ACR}_{\mathrm{exp},i} - \mathrm{ACR}_{\mathrm{sim},i}| \tag{5}$$

$$\mathrm{RPS}_{\mathrm{error,sum}} = \sum_{i=1}^{128} |\mathrm{RPS}_{\mathrm{exp},i} - \mathrm{RPS}_{\mathrm{sim},i}| \tag{6}$$

where $\mathrm{ACR}_{\mathrm{exp},i}$, $\mathrm{ACR}_{\mathrm{sim},i}$, $\mathrm{RPS}_{\mathrm{exp},i}$ and $\mathrm{RPS}_{\mathrm{sim},i}$ are amplitude ratio and relative phase shift of experiments and simulations respectively for each collection fibre, i.

3. Results and discussion

3.1. Influence of fibre length

Figure 3 reports a typical measurement of RPS for each collection fibre before (open symbol) and after (filled symbol) the removal of the systematic offset as determined from equation (1). The data shown were collected with GRIN lens collimation and are presented for excitation illumination at source number 9 for a target of 1 μM ICG concentration at 1.26 cm depth. In all future data presented, the systematic phase offsets were subtracted from the measurements to investigate the improvement of filter performance using GRIN lenses. Since fibre length does not significantly impact amplitude, no correction was made on I_{ac} and I_{dc} values.

3.2. Transmission ratio

Figure 4 shows typical transmission ratios, $R(I_{\mathrm{ac}})$ ((a) (b)) and $R(I_{\mathrm{dc}})$ ((c) (d)) with and without attached GRIN lenses as a function of fibre location on the breast phantom when fibre number 9 provided the modulated excitation illumination. At all collecting fibre locations, the transmission ratios for I_{ac} and I_{dc} with GRIN lenses were significantly lower than those without GRIN lenses due to the reduction of excitation light leakage. Significant differences at a confidence level of $\alpha = 0.05$ occurred between the mean transmission ratio computed from measurements made with and without GRIN lenses. Similar trends were found in the remaining 25 source locations (data not shown for brevity).

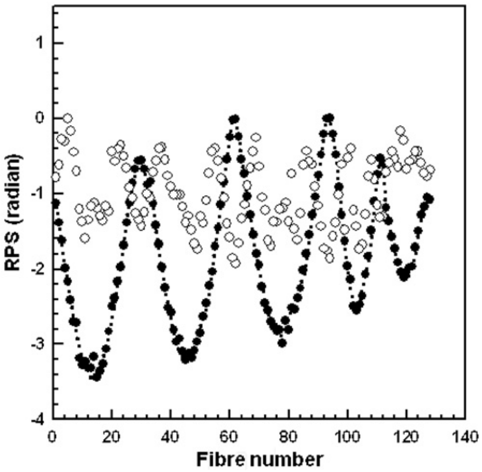

Figure 3. Comparison of RPS before (unfilled circles) and after (filled circles) fibre calibration as a function of collection fibre location based on a source position (source number 9). The dotted line represents RPS of forward model. Results are presented for data collected with GRIN lenses.

3.3. Model mismatch errors

3.3.1. Target depth study. Figure 5 shows typical data sets for the calibrated RPS corresponding to each collection fibre with and without GRIN lenses for source number 9 and for target depths of 1.26 (a), 2 (b), and 3 cm (c) and ICG concentration of 1 μM. The filled symbols denote data taken with GRIN lenses while open symbols denote that taken without GRIN lenses. The dotted curves represent lines connecting simulated RPS at each fibre position.

As shown in figures 5(a), (b), and (c), large model mismatch errors were found in RPS when GRIN lenses were not used. Because systematic offsets were already removed using the calibration technique as described in section 3.1, these errors can be assumed to be a result of excitation light leakage. For ACR, a good model match was observed between referenced measurements and simulations with and without GRIN collimation for all target depths (ACR graphs are not shown for brevity). Figure 6 reports the mean summation error of ACR (a) and calibrated RPS (b) for 128 collection fibres with (filled circles) and without (open circles) GRIN lenses as a function of target depth. The error bars represent the standard deviations of the summation errors of three sets of measurements resulting from illumination with source 9. Significant differences ($p < 0.005$) at a confidence level of $\alpha = 0.05$ occurred between the mean $\mathrm{ACR}_{\mathrm{error,\,sum}}$ and mean $\mathrm{RPS}_{\mathrm{error,\,sum}}$ computed from equations (5) and (6) with and without GRIN lenses as predicted by the hypothesis *t*-test (Montgomery and Runger 1999). For the remaining 25 fibre sources, similar trends were found (data not shown for brevity). As might be anticipated, the model mismatch was always higher when GRIN lenses were not used as compared to when they were used. Specifically, as a result of GRIN lens collimation, we reduced the $\mathrm{ACR}_{\mathrm{error,\,sum}}$ between 2 and 15% and the $\mathrm{RPS}_{\mathrm{error,\,sum}}$ between 82 and 85% for all target depths. Model mismatch errors increased for both ACR and RPS as a function of target depth, probably because weak fluorescent signals at deep target locations were increasingly dominated by the noise floor of excitation light leakage, however minimized by the use of the GRIN lenses.

Due to the fluorophore lifetime, the phase of collected emission light was found to be substantially larger than that collected at the excitable wavelength. Consequently, excitation

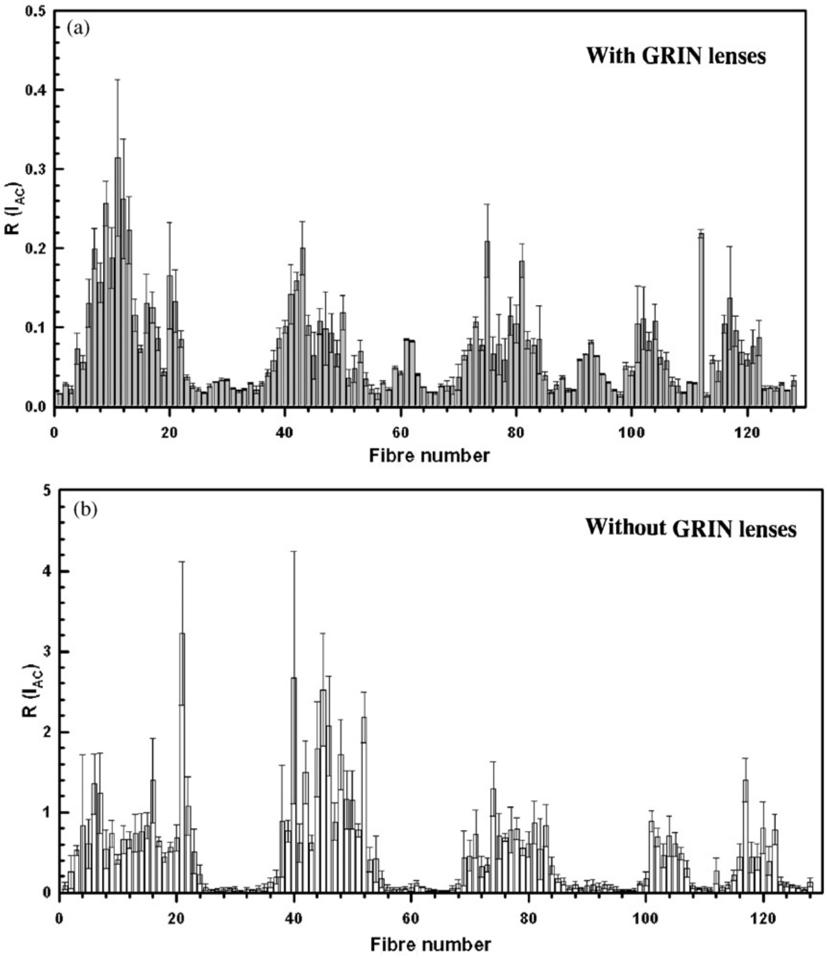

Figure 4. Comparison of transmission ratio with ((a) (c)) and without ((b) (d)) GRIN lens for I_{ac} ((a) (b)) and I_{dc} ((c) (d)) measurements based on a source position (source number 9). Filled and unfilled bars represent the transmission ratio with and without GRIN lens respectively. Error bars represent the standard deviation of transmission ratio with region of the collection fibre.

light leakage artificially decreases the RPS measurements of emission light. Depending upon the excitation fluence at the collecting fibre, the error in RPS can vary. It is noteworthy that across all the sources employed, we noted that the degree of model mismatch errors predicted by $|\mathrm{RPS}_{\mathrm{exp},i} - \mathrm{RPS}_{\mathrm{sim},i}|$ was correlated to the transmission ratio computed from equation (2). The slope of linear regression for the correlation plot between $\mathrm{RPS}_{\mathrm{error}}$ from figure 5(c) and $R(I_{ac})$ was 0.68 (correlation coefficient = 0.62, p-value < 0.0001) and Analysis of Variance (ANOVA) (Montgomery and Runger 1999) method was employed to determine the linear regression parameters, supporting the conclusion that the accuracy of measurements depended upon leakage of excitation light. In general, the attachment of GRIN lenses for collimation of collected light significantly improved the model match.

3.3.2. Target concentration study. Similar trends, as compared to those seen with increasing target depths, were found with decreasing target concentrations. Figure 7 reports the mean

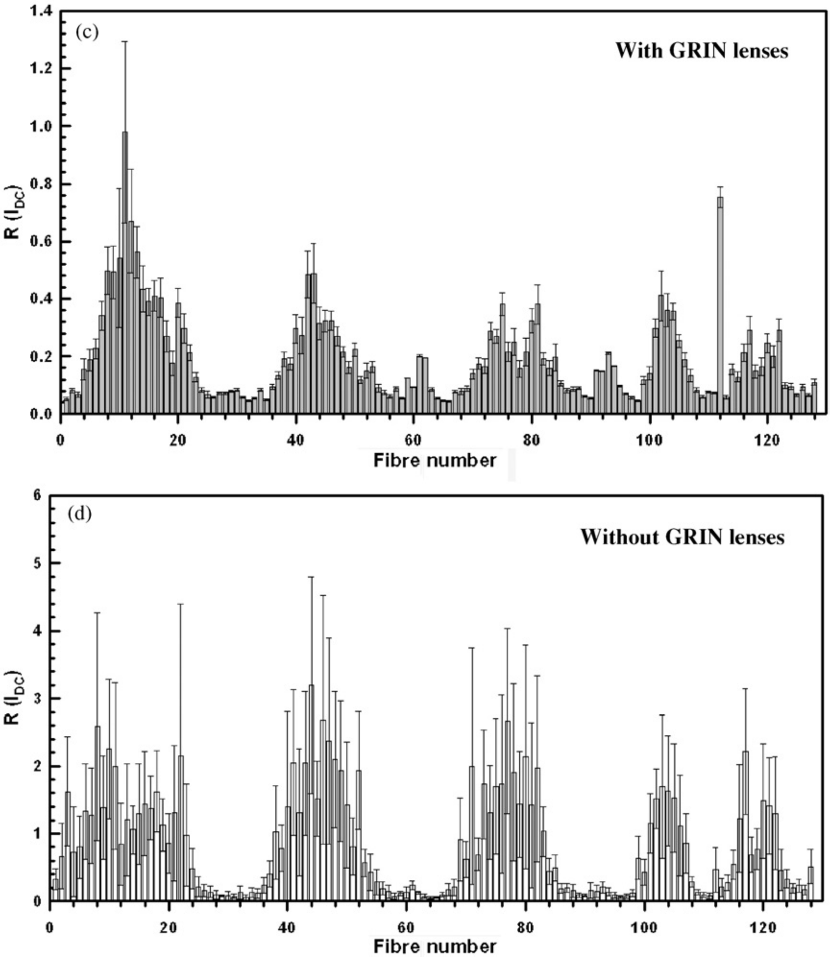

Figure 4. (Continued.)

summation error of ACR (a) and calibrated RPS (b) for 128 collection fibres with (filled circles) and without (open circles) GRIN lenses as a function of target concentration. The error bars represent the standard deviations of the summation errors of three sets of measurements resulting from illumination with source 9. Significant differences ($p < 0.005$) at a confidence level of $\alpha = 0.05$ occurred between the mean $\mathrm{ACR}_{\mathrm{error,\ sum}}$ and mean $\mathrm{RPS}_{\mathrm{error,\ sum}}$ computed from equations (5) and (6) with and without GRIN lenses as predicted by the hypothesis *t*-test (Montgomery and Runger 1999). For the remaining 25 fibre sources, similar trends were found (data not shown for brevity). As shown in figure 7, model mismatch errors increased as target concentration decreased for both ACR and RPS. Additionally, the model match associated with measurements made using the GRIN lens (filled symbols) was improved when compared to that without the GRIN lens (open symbols). The simple addition of GRIN lenses resulted in a reduction between 2 and 21% of $\mathrm{ACR}_{\mathrm{error,\ sum}}$ and 56 and 83% of $\mathrm{RPS}_{\mathrm{error,\ sum}}$ for all target concentrations. Consequently, GRIN lens collimation was more effective in improving model match of RPS than that of ACR.

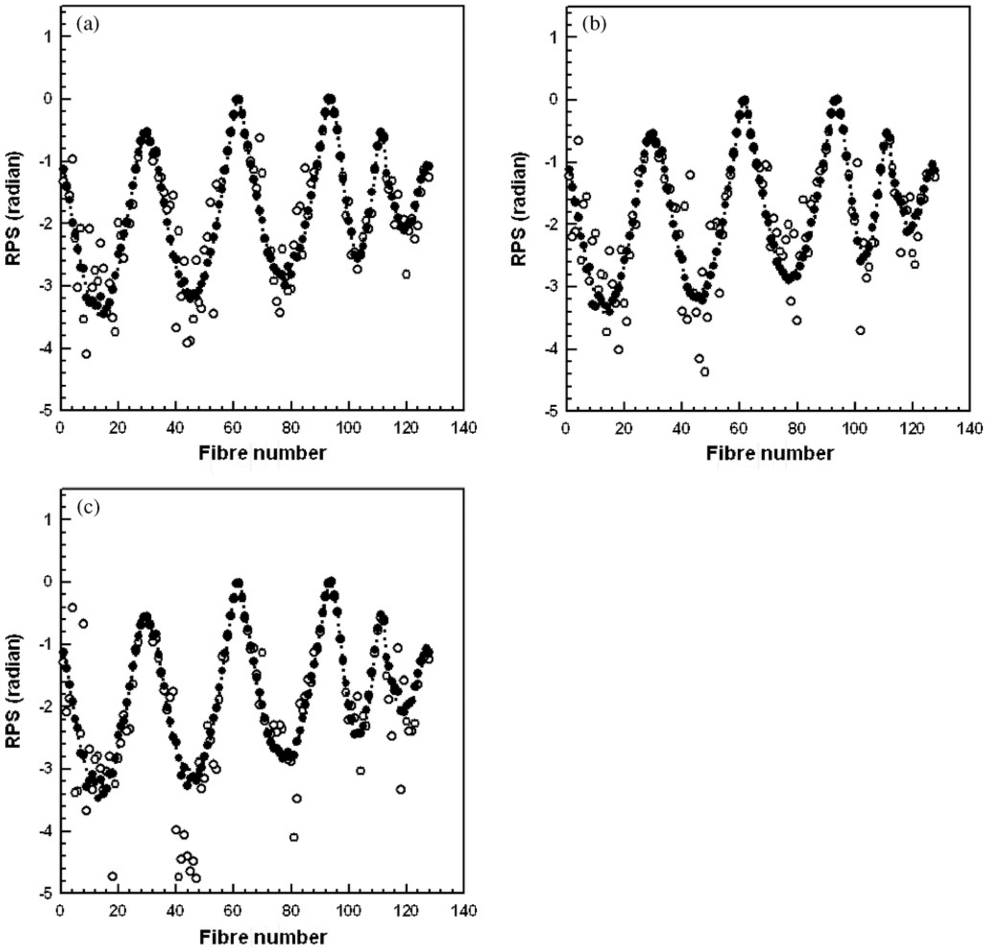

Figure 5. Comparison of relative phase difference (RPS) between measurements (symbols) and forward model (dotted line) for a source location (source number 9) as a function of fibre position. The filled circles denote measurements with GRIN lenses while the unfilled symbols denote those without. Target centroid depth varied from 1.26 cm (a), 2 cm (b), and 3 cm (c) at 1 μM ICG concentration.

4. Summary

In general, the accuracy of fluorescence enhanced optical imaging and tomography depends on extracting a small fluorescent signal from an overwhelming and multiply scattered excitation signal. Factors such as fluorophore concentration and target depth impact the relative amount of fluorescence and excitation light collected. While the use of NIR excitable fluorophores minimizes the background owing to autofluorescence, significant background can arise from excitation light leakage through filters. Since maximal performance of interference filters depends upon normally incident excitation light, multiple scattering is especially confounding. For example, in the breast phantom geometry in which the 1 cm^3 target of 1 μM ICG concentration located 1 cm deep within a medium with TBR of 100:1, a weak emission fluence of 4.14×10^{-8} (photons (cm^2 s)$^{-1}$) can be overwhelmed by a strong excitation fluence

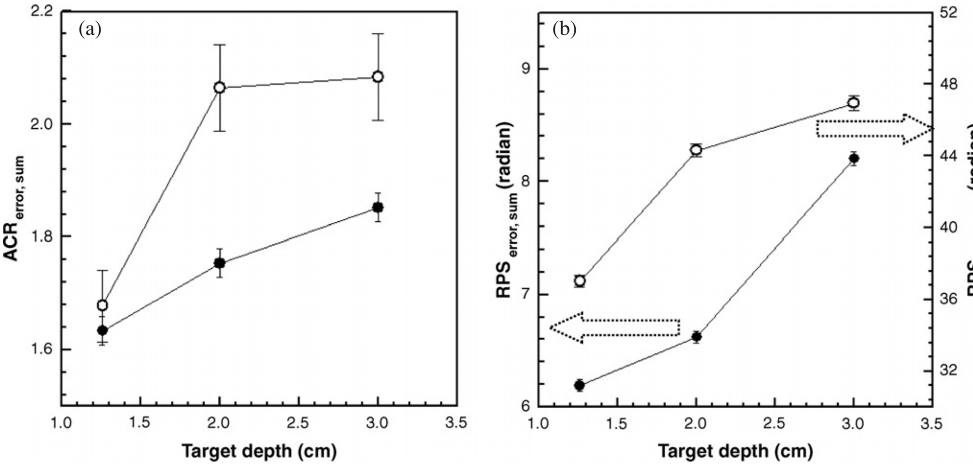

Figure 6. Comparison of mean of ACR (a) and RPS (b) errors between with and without GRIN lens as a function of target depth. Filled and unfilled circles correspond to the mean mismatch errors with and without GRIN lens respectively. Error bars represent the standard deviation of mean mismatch errors.

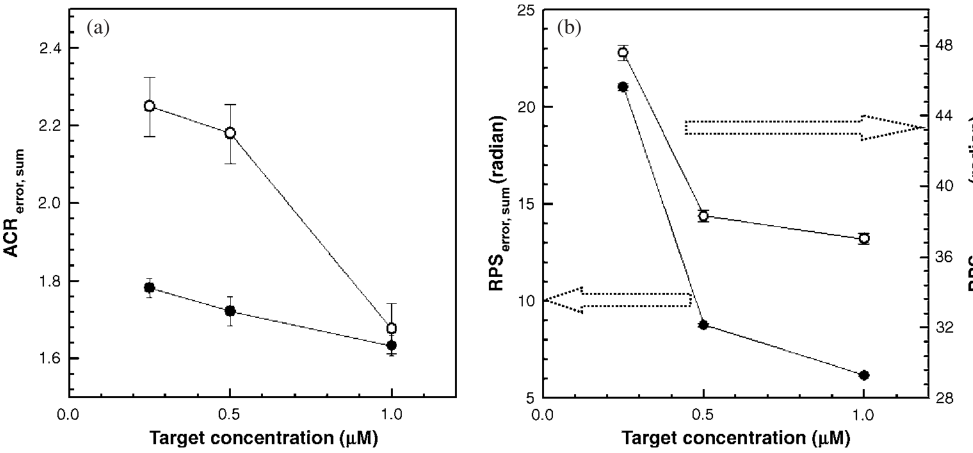

Figure 7. Comparison of mean of ACR (a) and RPS (b) errors between with and without GRIN lens as a function of target concentration. Filled and unfilled circles correspond to the mean mismatch errors with and without GRIN lens respectively. Error bars represent the standard deviation of mean mismatch errors.

of 2.92×10^{-5} (photons (cm^2 s) $^{-1}$). The order of magnitude difference between excitation and emission fluence only increases with target depth, and with reduction in target fluorophore concentration. One means to reduce excitation light leakage is to collimate light prior to filtering so that it is normally incident on the interference filters. When using fibre optics to collect point measurements of fluence for tomographic reconstructions, GRIN lenses enable collimation of all emitted light thereby minimizing excitation light leakage. On the other hand, when employing direct, planar imaging where the emission light across an area is collected, the image plane can be collimated before passing through the interference filters (Hwang *et al*

2005). However, it is nearly impossible to collimate all multiply scattered light in these area detection systems. An added strategy may be to use cross polarizers to additionally eliminate the specularly reflected excitation light, which constitutes a substantial portion of the collected excitation light (Thompson *et al* 2003, Joshi *et al* 2006). Nonetheless, the use of GRIN lenses for fibre optic collection of light represents the most efficient manner to collect propagated light and separate emission from excitation contribution. Our contribution shows that the improvement of model match by the adoption of GRIN lens optics is due to the improvement of optical filter performance. While the addition of optical components may enhance excitation light rejection at the expense of total photon budget, it is important to note that carefully chosen detection schemes, as employed with the homodyned measurements coupled with the integrating CCD camera used herein, enable one to simply increase the integration times to compensate for a reduced photon budget. The attenuation losses associated with GRIN lenses in this study are minimal and do not require increased integration times. The improvement in model mismatch should contribute to increased accuracy in image reconstruction as described in objective assessment of image quality (Sahu *et al* 2006), as well as ongoing tomographic reconstructions from actual experimental measurements.

Acknowledgment

We acknowledge financial support for this work by the National Institute of Health (R01 CA112679).

References

Achilefu S, Dorshow R B, Bugaj J E and Rajagopalan R 2000 Novel receptor-targeted fluorescent contrast agents for *in vivo* tumor imaging *Invest. Radiol.* **35** 479–85

Eppstein M J, Dougherty D E, Troy T L and Sevick-Muraca E M 1999 Biomedical optical tomography using dynamic parameterization and Bayesian conditioning on photon migration measurements *Appl. Opt.* **38** 2138–50

Godavarty A, Zhang C, Eppstein M J and Sevick-Muraca E M 2004 Fluorescence-enhanced optical imaging of large phantoms using single and simultaneous dual point illumination geometries *Med. Phys.* **31** 183–90

Houston J P, Ke S, Wang W, Li C and Sevick-Muraca E M 2005 Quality analysis of *in vivo* near-infrared fluorescence and conventional gamma images acquired using a dual-labeled tumor-targeting probe *J. Biomed. Opt.* **10** 054010

Houston J P, Thompson A B, Gurfinkel M and Sevick-Muraca E M 2003 Sensitivity and depth penetration of continuous wave versus frequency-domain photon migration near-infrared fluorescence contrast-enhanced imaging *Photochem. Photobiol.* **77** 420–30

Hwang K, Houston J P, Rasmussen J C, Joshi A, Ke S, Li C and Sevick-Muraca E M 2005 Improved excitation light rejection enhances small-animal fluorescent optical imaging *Mol. Imaging* **4** 194–204

Joshi A, Bangerth W, Hwang K, Rasmussen J C and Sevick-Muraca E M 2006 Plane-wave fluorescence tomography with adaptive finite elements *Opt. Lett.* **31** 193–5

Joshi A, Bangerth W and Sevick-Muraca E M 2004 Adaptive finite element based on tomography for fluorescent optical imaging in tissue *Opt. Express* **12** 5402–17

Li X D, Chance B and Yodh A G 1998 Fluorescence heterogeneities in turbid media, limits for detection, characterization, and comparison with absorption *Appl. Opt.* **37** 6833–43

Licha K 2002 Contrast agents for optical imaging *Top. Curr. Chem.* **222** 1–29

Lin Y, Weissleder R and Tung C 2002 Novel near-infrared cyanine fluorechromes: synthesis, properties and bioconjugation *Bioconjugate Chem.* **13** 605–10

Montgomery D C and Runger G C 1999 *Applied Statistics and Probability for Engineers* 2nd edn (New York: Wiley) p 375

Pham W, Lai W, Weissleder R and Tung C 2003 High efficiency synthesis of a bioconjugatable near-infrared fluorochrome *Bioconjugate Chem.* **14** 1048–51

Reynolds J, Troy T L and Sevick-Muraca E M 1997 Multipixel techniques for frequency-domain photon migration imaging *Biotech. Prog.* **13** 669–80

Sahu A, Joshi A, Kupinski M A and Sevick-Muraca E M 2006 Assessment of a fluorescence-enhanced optical imaging system using the Hotelling observer *Opt. Express* **14** 7642–60

Sahu A, Roy R, Joshi A and Sevick-Muraca E M 2005 Evaluation of anatomical structure and nonuniform distribution of imaging agent in near-infrared fluorescence-enhanced optical tomography *Opt. Express* **13** 10182–99

Sakamoto T 1993 Analytic solutions of the eikonal equation for a GRIN-rod lens *J. Mod. Opt.* **40** 503–16

Sevick-Muraca E M, Chance B, Leigh J, Nioka S and Maris M 1991 Quantitation of time-resolved and frequency-resolved optical-spectra for the determination of tissue oxygenation *Anal. Biochem.* **195** 330–51

Sevick-Muraca E M, Lopez G, Troy T L, Reynolds J S and Hutchinson C L 1997 Fluorescence and absorption contrast mechanism for biomedical optical imaging using frequency-domain techniques *Photochem. Photobiol.* **66** 55–64

Thompson A B, Hawrysz D J and Sevick-Muraca E M 2003 Near-infrared fluorescence contrast-enhanced imaging with area illumination and area detection: the forward imaging problem *Appl. Opt.* **42** 4125–36

Thompson A B and Sevick-Muraca E M 2002 NIR fluorescence contrast enhanced imaging with ICCD homodyne detection: measurement precision and accuracy *J. Biomed. Opt.* **8** 111–20